ACSNANO

www.acsnano.org

ARTICLE

n Situ 2D MoS_2 Field E ect Transistors with an Electron Beam Gate

Paul Masih Das and Marija Drndic

Cite This: *CS Nano* 2020 14 7389 7397

Read Online

CCESS | Metrics More | Article Recommendations | Supporting Information

ABSTRACT: We use the beam of a transmission electron microscope (TEM) to modulate *in situ* the current voltage characteristics of a two-terminal monolayer molybdenum disul de (MoS_2) channel fabricated on a silicon nitride substrate. Suppression of the two-dimensional (2D) MoS_2 channel conductance up to 94 is observed when the beam hits and charges the substrate surface. Gate-tunable transistor characteristics dependent on beam current are observed even when the beam is up to tens of microns away from the channel. In contrast, conductance remains constant when the beam passes through a micron-sized hole in the substrate. There is no MoS_2 structural damage during gating, and the conductance reverts to its original value when the beam is turned off. We observe on/off ratios up to ~60 that are largely independent of beam size and channel length. This TEM eld-effect transistor architecture with electron beam gating provides a platform for future *in situ* electrical measurements.

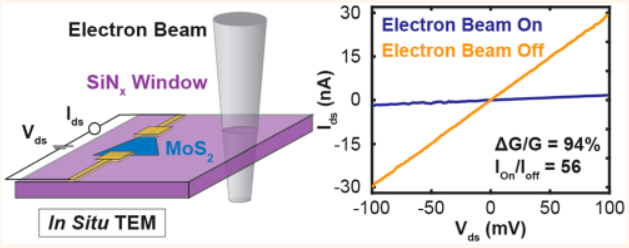

KEYWORDS: *in situ transmission electron microscopy transition metal dichalcogenides eld-effect transistor electronic transport silicon nitride molybdenum disul de*

Transmission electron microscopy (TEM) o ers an ideal platform for the structural and analytical analysis of atomically thin two-dimensional (2D) materials.[1 7] *In situ* studies that combine the atomic-resolution capabilities of TEM with the growing array of electrochemistry, gas/fluid flow, and high/low-temperature TEM holders have emerged as powerful tools for 2D nanoscale characterization.[8 11] However, methods for *in situ* electrical biasing have seen little development and are currently limited to two terminal measurements as conventional architectures consisting of metallic back or top gates are not readily electron transparent.[12,13] Several *in situ* devices including an electrical gate (*i.e.*, third terminal) have previously been demonstrated. For example, Kim *et al.* fabricated carbon nanotube (CNT) field-e ect transistors (FETs) containing slits that allow for simultaneous transport measurements and TEM imaging.[14] Similarly, Rodriguez-Manzo *et al.* showed that a free-standing graphene side gate could be used to modulate the conductance in a graphene nanoribbon (GNR) spaced up to 100 nm away.[15] These techniques involve relatively complex fabrication procedures and result in a weak, spatially nonuniform gating e ect.

Previous *in situ* TEM works have also utilized direct electron beam irradiation of suspended as well as on-substrate 2D materials to modulate two-terminal conductance, for example, in graphene,[15 18] MoS_2,[19] and WS_2.[20] Although conductance is generally suppressed due to 2D material damage from beam exposure, *in situ* TEM Joule heating from the electrical current between the source and drain electrodes was used to induce recrystallization of the 2D lattice and cause a conductance increase.[15 18,20] Despite these reconstructions, techniques involving direct interactions between the electron beam and 2D material introduce some degree of irreversible damage, which results in a permanent change in electronic properties. Additional e orts are therefore needed to produce platforms for *in situ* electrical biasing with a robust, tunable, and position-controlled gate parameter.

Here, we report the *in situ* electrical gating of 2D MoS_2 channels by targeting the electron beam of a TEM at controlled positions on a silicon nitride (SiN_x) window. The main features of 2D channel gating by the electron beam are summarized as follows. Devices consist of a two-terminal monolayer transition metal dichalcogenide (TMD) geometry supported on a SiN_x window. When the electron beam is turned on and hits the insulating substrate of the transistor

Received: April 6, 2020
Accepted: May 7, 2020
Published: May 7, 2020

https://dx.doi.org/10.1021/acsnano.0c02908
CS Nano 2020 14 7389 7397

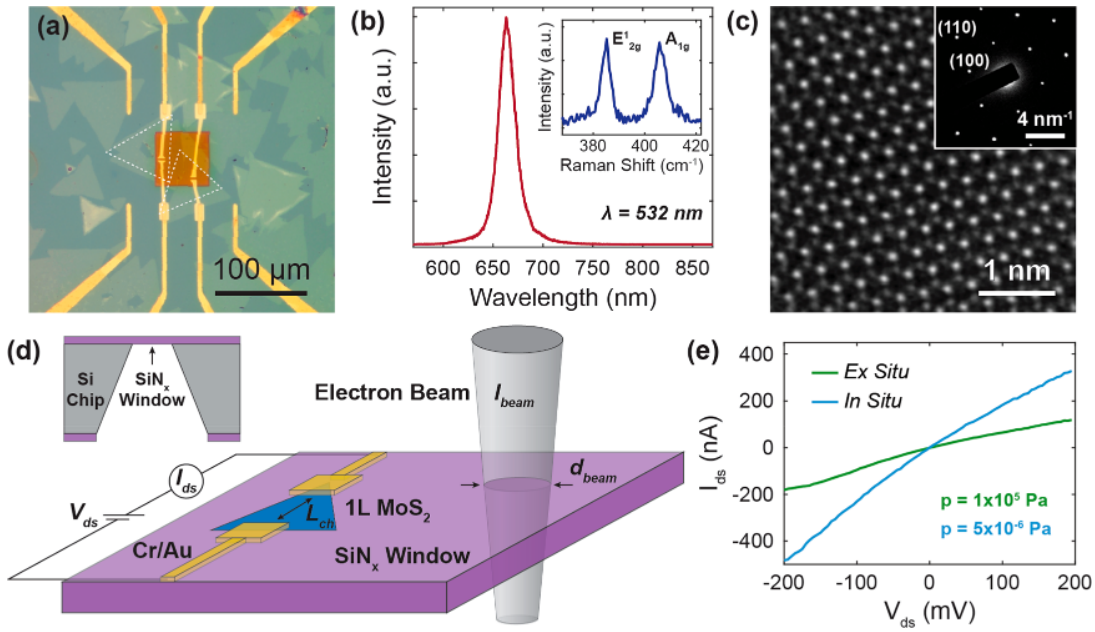

Figure 1. TEM-FET device architecture, current voltage measurement, and MoS_2 Raman and TEM characterization. (a) Optical image of monolayer MoS_2 flakes (outlined in white) transferred onto a 60 m square SiN_x window (orange) with top-contacted Cr/Au metallic leads (yellow). (b) Photoluminescence and (inset) Raman spectra of MoS_2 under an excitation wavelength of 532 nm. The PL peak at 660 nm and Raman mode separation ($\omega_{A_{1g}}$ $\omega_{E_{2g}}$) of 20 cm ^{1} are indicative of monolayer thickness. (c) High-angle annular dark- eld STEM lattice image and (inset) selected area electron diffraction pattern of monolayer 2H-phase MoS_2 showing rst-order (100) and second-order (110) reflections. (d) Device con guration showing electron beam (gray) exposure on a 100 nm thick SiN_x window containing a two-terminal MoS_2 device. V_{ds}, I_{ds}, L_{ch}, I_{beam}, and d_{beam} correspond to drain source voltage, drain source current, channel length, electron beam current, and electron beam diameter in the specimen plane, respectively. (Inset) The SiN_x window sits in the center of a 290 m thick Si chip (3 mm 5 mm). Additional fabrication details can be found in Supporting Information Figure S2. (e) *x situ* and *in situ* I_{ds} V_{ds} curves for a MoS_2 TEM-FET at pressure levels of 1 10^5 and 5 10 ^{6} Pa, respectively, with the electron beam turned off.

chip, even up to 50 m away from the device channel, conductance of the 2D channel changes and gating occurs due to substrate charging. As long as the beam does not hit the 2D channel material itself, this conductance modulation is completely reversible and there is no device hysteresis or structural damage to the 2D material. Gating is controlled by tuning the strength of the TEM condenser lens (*i.e.*, spot size), which results in electron beam currents between 0 and 70 nA in this study. We observe 2D channel current on/o ratios up to ~60 that are approximately independent of beam position relative to the 2D channel, beam size, and other parameters over the time scales of our measurements.

Importantly, we establish that there is no change in the 2D channel conductance when the beam passes near the channel but through vacuum and has no interaction with the chip, as there is no SiN_x substrate charging. This measurement was successfully performed by intentionally drilling a 1 m size hole in the SiN_x membrane near the 2D channel using focused ion beam (FIB) milling and targeting the electron beam through its center. Similarly, no gating is observed when the beam is positioned to hit the outside of the TEM-transparent, 100 nm thick suspended SiN_x window region, suggesting that charges are dissipated through the conductive Si support chip so that no significant charging occurs. *In situ* charging and discharging of the SiN_x substrate are additionally monitored by time-dependent current voltage measurements in the 2D channel. After turning the electron beam o , the current in the 2D channel displays an exponential-like rise, 1 exp(t/τ), as the substrate discharges with a characteristic time constant of τ ~ 100 s.

RESULTS AND DISCUSSION

Figure 1a shows an optical image of the TEM-FET device consisting of monolayer 90 100 m large MoS_2 flakes deposited onto a 100 nm thick, 60 m wide SiN_x window. The electron-transparent window is located in the center of a 3 mm by 5 mm Si/SiN_x chip (Figure 1d inset). The MoS_2 crystals utilized in this study were grown through chemical vapor deposition (CVD). The photoluminescence (PL) spectrum of as-grown MoS_2 in Figure 1b exhibits a narrow peak at ~1.88 eV that is consistent with monolayer thickness.[21] Likewise, the frequency separation of ~20 cm ^{1} between the in-plane E^1_{2g} and out-of-plane A_{1g} phonon modes agrees well with expected values for monolayer MoS_2 under a 532 nm excitation (Figure 1b inset).[22] Dark-field scanning TEM (STEM) lattice imaging and selected area electron di raction (SAED) patterns indicate a hexagonal 2H phase structure, which is a relatively stable, well-characterized semiconductor compared to the metallic 1T phase (Figure 1c).[23,24]

The electrical measurement setup inside the TEM is shown schematically in Figure 1d. The MoS_2 flake is contacted through two-terminal Cr/Au leads and an *in situ* electrical biasing TEM holder to an external source meter. Electron beam lithography and 2D flake growth and transfer details can be found in the Methods and Supporting Information Figure S2. The 200 keV electron beam used in this study is precisely positioned on the device surface by moving the TEM sample stage. We present results showing how the measured drain source current (I_{ds}) with an applied drain source voltage (V_{ds}) across the MoS_2 channel of length L_{ch} is gated when changing

https://dx.doi.org/10.1021/acsnano.0c02908
CS Nano 2020 14 7389 7397

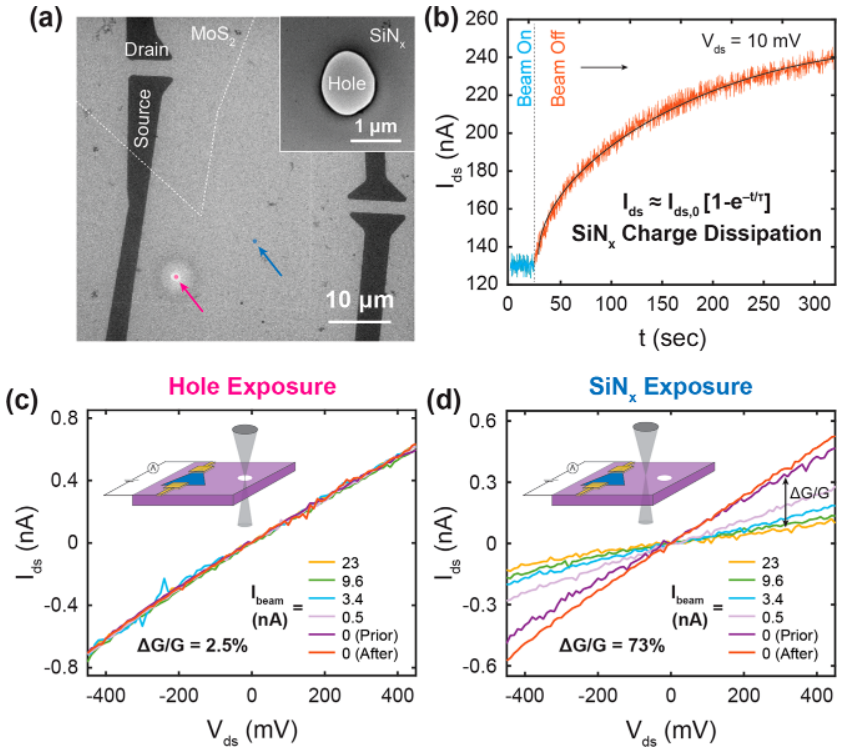

Figure 2. Charging of the SiN_x substrate using the electron beam causes MoS_2 gating and the absence of gating if the electron beam is passing through a micron-size hole in the substrate. (a) Low-magni cation TEM image of a TEM-FET SiN_x window containing a 1.2 m diameter FIB hole indicated by the pink arrow. The pink and blue dots show the location of the electron beam during I_{ds} V_{ds} measurements in (c,d), respectively. (Inset) High-magni cation TEM image of the hole. (b) Continuous DC measurement of I_{ds} in a TEM-FET over a period of 5 min under a constant V_{ds} = 10 mV. After turning the electron beam off (orange), the device current increases and is indicative of electronic charge dissipation. The limited exponential t is shown as a solid black line. (c,d) I_{ds} V_{ds} curves when a focused electron beam (d_{beam} = 10 nm) is placed (c) through the FIB hole and (d) on the SiN_x window at the locations marked by the pink and blue arrows, respectively, in panel (b). The insets in (c,d) provide schematics of the exposure conditions. Conductance, G, is taken as the slope of each I_{ds} V_{ds} curve. Conductance change, G/G, is taken as the percent change between the G values of the purple (I_{beam} = 0 nA) and yellow (I_{beam} = 23 nA) curves, respectively. No gating effect (G/G = 2.5) is observed in the hole exposure condition, which highlights the crucial role of the SiN_x substrate in creating a tunable eld effect.

the TEM beam current (I_{beam}), beam diameter (d_{beam}), and its position relative to the 2D channel. The magnitude of I_{beam} is controlled in the TEM by tuning the strength of condenser lens 1 (CL1), typically referred to as "spot size". Data presented include results from multiple (>200) continuous DC and I_{ds} V_{ds} measurements on five MoS_2-based devices that were electrically characterized in the TEM and gated by the TEM beam. Whereas the magnitude of I_{ds} was observed to be di erent across devices due to di erences in contact resistance, similar degrees of gating and current suppression were seen (for example, see Supporting Information Figures S4 and S5).

As shown in Figure 1e, the two-terminal monolayer MoS_2 device exhibits a nonlinear I_{ds} V_{ds} curve under ambient *ex situ* conditions (pressure $p = 1 \times 10^5$ Pa). When placed in the column of the TEM ($p = 5 \times 10^{-6}$ Pa), an increase in I_{ds} is observed. This has previously been demonstrated in conventional back-gated MoS_2 FETs measured in air and in vacuum and was attributed to the desorption of gas molecules at the TMD metal interface in vacuum, which causes a lowering of the Schottky barrier and improved charge carrier injection.[25] The high vacuum condition of the TEM column ($p = 5 \times 10^{-6}$ Pa) is advantageous for producing near-ohmic behavior in TEM-FETs.

Figure 2a is a TEM image of one of the devices tested, with the indicated source and drain electrodes and the outline of the 2D MoS_2 flake deposited on top and between the electrodes. We designed and fabricated this TEM-FET device to also contain a 1.2 m diameter FIB hole in the SiN_x window, with a high-magnification TEM image of the hole region shown in the inset of Figure 2a. The hole is also marked by a pink arrow in Figure 2a and is located about 6 m away from the edge of the source electrode. This hole was fabricated with ion beam milling using a 30 keV Ga^+ FIB after the other parts of the device were assembled. By moving the sample stage *in situ*, the location of the electron beam is precisely guided to expose di erent locations on the device.

In the *hole exposure* experiment, the TEM beam with d_{beam} = 10 nm was positioned to pass through the center of the hole in Figure 2a (pink dot) so that the beam traveled only through the vacuum and did not have direct physical contact with the SiN_x surface. In the *SiN_x exposure* experiment, the beam was positioned to impinge directly onto the SiN_x surface; this beam location is indicated by the blue dot in Figure 2a. In both experiments, an I_{ds} V_{ds} curve is first acquired with the electron beam turned o (*i.e.*, closed beam valve). After turning on the beam at the specified position and waiting 3 5 s, a series of four I_{ds} V_{ds} measurements were taken, each with a di erent beam current: I_{beam} = 0.5, 3.4, 9.6, and 23 nA. The I_{ds} V_{ds} measurements take 10 12 s each and are obtained in random order to reduce sampling bias and systematic errors (see

https://dx.doi.org/10.1021/acsnano.0c02908
CS Nano 2020 14 7389 7397

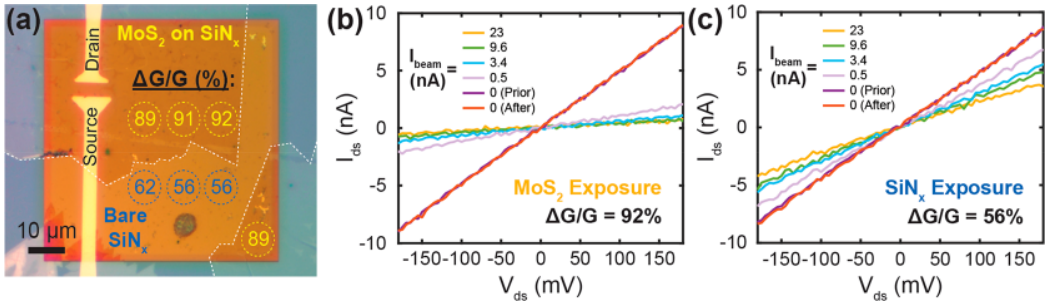

Figure 3. Current voltage measurements of MoS_2 for several different positions of the electron beam on the insulating SiN_x substrate. (a) Optical image of a TEM-FET showing G/G ( ) values as a function of electron beam position on the SiN_x window. Each number corresponds to a G/G value ( ) obtained while the encircled area (dashed circle) was exposed to a TEM beam (d_{beam} = 8.7 m). Yellow and blue values correspond to exposure on areas of the SiN_x window with and without monolayer MoS_2 (outlined in white), respectively. Due to a stronger eld effect, higher G/G values are observed when the electron beam is parked on a region containing MoS_2. (b) Example I_{ds} V_{ds} curves for electron beam exposure on a bare SiN_x window with G/G = 56 . (c) I_{ds} V_{ds} curves under electron beam exposure to an MoS_2-covered region with resulting G/G = 92 . I_{ds} V_{ds} curves for all locations indicated in panel (a) can be found in Supporting Information Figure S4.

Methods), whereas a negligible leakage current (< 500 pA) was observed through the SiN_x membrane (see also current voltage curves in Figure 4). The beam is subsequently turned o , and after 3 5 s, another I_{ds} V_{ds} curve is acquired.

Figure 2c,d shows the corresponding I_{ds} V_{ds} traces for I_{beam} = 0.5 (pink), 3.4 (blue), 9.6 (green), and 23 (yellow) nA. Curves taken with the electron beam o (I_{beam} = 0 nA) prior to and after these measurements are also given (purple and red curves, respectively). From the slope of each I_{ds} V_{ds} trace, we calculate the two-terminal device conductance given by

$$G = \frac{I_{ds}}{V_{ds}}$$

Figure 2c shows that when the beam is passing straight through the hole (*i.e., hole exposure*), the device conductance remains virtually unchanged. A di erence in TEM-FET conductance due to the electron beam occurs *only* when it hits the SiN_x surface and can be quantified through

$$\frac{\Delta G}{G}(\%) = \frac{G_{I_{beam}=0\ nA} - G_{I_{beam}=23\ nA}}{G_{I_{beam}=0\ nA}}$$

where $G_{I_{beam}=0\ nA}$ and $G_{I_{beam}=23\ nA}$ are the conductance values measured under beam currents of 0 and 23 nA, respectively. In the *SiN_x exposure* experiment (Figure 2d), a significant $\Delta G/G$ value of 73 is observed when the beam hits the SiN_x surface. Specifically, the conductance is at the maximum when the electron beam is o (I_{beam} = 0 nA). As I_{beam} increases and more electrons hit the SiN_x per unit time over a fixed beam area (up to 1.8 × 10^9 electrons/s·nm^2), the conductance decreases, yielding a minimum conductance for the maximum beam current, I_{beam} = 23 nA. Direct interaction between incident electrons and a suspended SiN_x window generates an additional electrostatic field and current suppression in the MoS_2 channel. We utilize this phenomenon for further *in situ* gating of the 2D TEM-FET devices and explain it below in more detail.

When the drain source voltage (V_{ds}) is fixed and the beam is turned on or o , it takes some time for the 2D channel conductance to respond to this event and asymptotically reach some equilibrium value. This is illustrated by the measurement in Figure 2b on the same device, where we monitor I_{ds} as a function of time under a fixed drain source voltage of 10 mV. The TEM beam with I_{beam}= 3.4 nA is first placed at the location on the SiN_x window indicated by the blue dot in Figure 2a, about 30 m away from the MoS_2 channel. Under this electron beam exposure for 30 s, the drain source current I_{ds} was first constant (blue curve). When the beam was subsequently turned o (*i.e.*, beam valve closed), I_{ds} initially increases rapidly before nearly leveling o over a period of 5 min (orange curve).

The current *versus* time is well described by a limited exponential growth over time:

$$I_{ds}(t) = I_{ds,0}[1 - e^{-t/\tau}]$$

where t is time, τ is a characteristic time constant, and $I_{ds,0}$ is the steady-state current value. Here, we obtain $\tau \sim 105$ s. The black line in Figure 2b shows a fit of this model to the experimental I_{ds} t data. This is consistent with previous studies that observed exponential behavior for charging in SiN_x[26] and suggests the insulating SiN_x substrate undergoes discharging when the beam is turned o . Similar behavior is also observed when the electron beam is turned on and the 2D channel current decreases exponentially, 1 + exp(t/τ), as the SiN_x substrate is charged by the impinging electron beam (Supporting Information Figure S3).

In general, electron exposure in TEM specimens results in radiation damage through primarily two modes: knock-on collisions and radiolysis.[27 29] Electrically insulating materials such as SiN_x also experience significant electrostatic charge accumulation. When exposed to the TEM beam, the ejection of secondary and Auger electrons from the insulating specimen leads to a charge imbalance.[29] This electron-deficient, hole-rich SiN_x membrane subsequently acquires a positive surface potential relative to the MoS_2 flake, leading to current modulation in the 2D channel. In the case of TEM-FETs here (see Figure 1a), stronger electron beam exposure results in a more electron-deficient membrane and therefore a larger gating e ect. A full discussion of electron SiN_x interactions that have been studied here can be found in Supporting Information section S1.[30 32]

In order to characterize the gating behavior in the MoS_2 TEM-FET by the electron beam, we next varied the beam location across the window. Figure 3a is an optical image of a TEM-FET device with a monolayer MoS_2 flake outlined in white. A broad TEM beam with a constant d_{beam} = 8.7 m was

https://dx.doi.org/10.1021/acsnano.0c02908
ACS Nano 2020 14 7389 7397

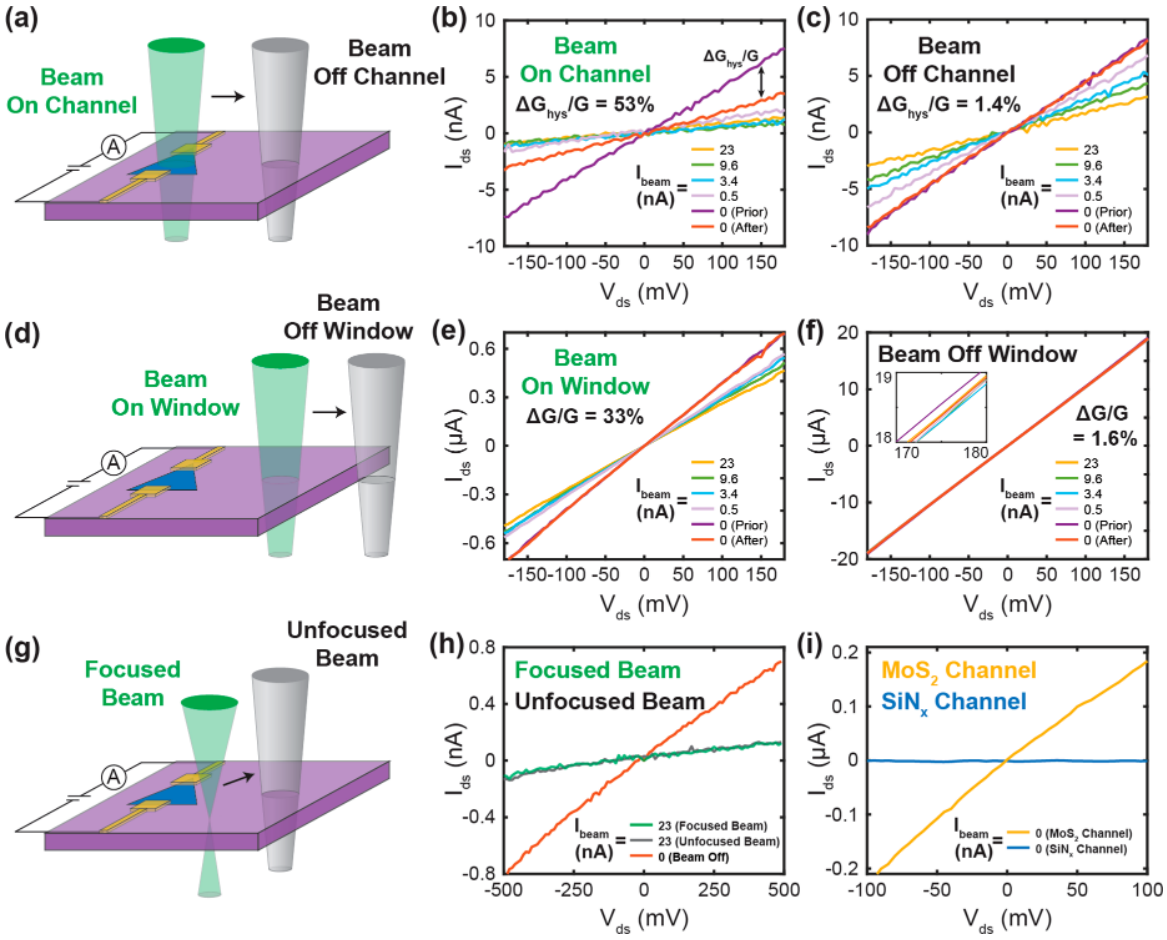

Figure 4. TEM-FET current voltage characterization as a function of beam position and size: on and off the MoS_2 channel, on and off the suspended SiN_x region, and focused *vs* unfocused illumination. (a) Schematic and (b,c) transport characteristics when the electron beam is parked on (green) and off (black) the MoS_2 device channel (gray). Electron beam exposure to the transistor channel results in a degree of hysteresis ($G_{hys}/G = 53$) due to the irreversible damage to the MoS_2 from the creation of sulfur vacancies in the conduction region. (d) Schematic and (e,f) I_{ds} V_{ds} curves for on- (green) and off-window (black) electron beam irradiation. Compared to exposure on the window ($G/G = 33$), a negligible degree of gating ($G/G = 1.6$) is seen when the beam is placed off the window because of the absence of an electric eld. (g) Schematic and (h) electronic characteristics of focused (green, $d_{beam} = 10$ nm) and unfocused (gray, $d_{beam} = 8.7$ m) beam placement on the TEM-FET window. No difference in conductance is observed between the two conditions. (i) I_{ds} V_{ds} curves for separate two-terminal devices with MoS_2 (yellow) and bare SiN_x (blue) channels. Electronic current is only detected through MoS_2 material.

positioned at seven locations indicated by dashed circles on both the MoS_2 flake (yellow) and the bare SiN_x window (blue). We note that the electron beam was mainly situated on the *source* side of the MoS_2 channel (Figure 3a) such that further experiments are needed to study the similarities and di erences in $\Delta G/G$ when placing the beam on the *drain* side. A comparison between tightly focused and broad beam exposure conditions is provided in Figure 4h. A series of I_{ds} V_{ds} curves for di erent I_{beam} were obtained at each location (see also Supporting Information Figure S4), with the resulting $\Delta G/G$ ( ) values displayed in Figure 3a. We observe no correlation between $\Delta G/G$ and the distance of the electron beam from the MoS_2 channel. For example, the beam locations closest to (7.7 m) and farthest from (52 m) the channel both display $\Delta G/G = 89$ (Figure 3a).

However, conductance suppression is observed to be significantly stronger when the electron beam is incident on MoS_2 compared to the bare SiN_x substrate. We note that the exposed MoS_2 is outside of the transistor channel region, a feature which will be discussed later (see Figure 4). Figure 3b,c shows I_{beam}-dependent I_{ds} V_{ds} data for electron beam exposure to MoS_2 and bare SiN_x, respectively. Although traces with the beam o ($I_{beam} = 0$ nA) are nearly identical, MoS_2 channel currents with the beam on ($I_{beam} \neq 0$ nA) are substantially lower when the MoS_2 region is exposed (Figure 3b). As shown in Figure 3a, this behavior is consistent across the TEM-FET, with average $\Delta G/G$ values of 90 (± 1.3) at MoS_2 exposure locations and 58 (± 2.8) on SiN_x. Therefore, $\Delta G/G$ is relatively constant across the extent of the TEM-FET and is amplified when the electron beam interacts with the semiconducting MoS_2 layer on the insulating window. We also note that negligible di erences in $\Delta G/G$ are observed between cases where the exposed MoS_2 flake is contacted to the source/drain and when it is electrically isolated (see Supporting Information Figure S5), suggesting that charge carrier injection from the electron beam to the MoS_2 device channel is insignificant.

In order to accurately quantify the ability of TEM-FET devices to return to their initial conductance values after gating with the electron beam (*i.e.*, hysteresis), we introduce the

https://dx.doi.org/10.1021/acsnano.0c02908
CS Nano 2020 14 7389 7397

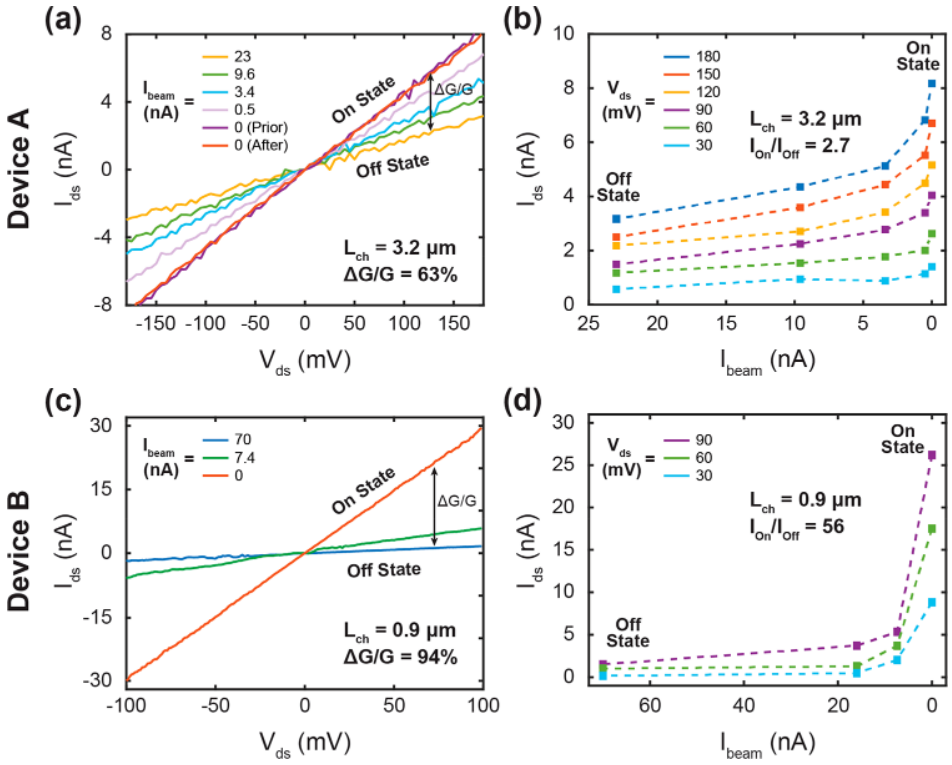

Figure 5. ***In situ*** **current voltage curves and on/off gating characteristics of MoS_2-based TEM-FETs. (a) I_{ds} V_{ds} curves as a function of I_{beam} for a MoS_2 device with L_{ch} = 3.2 m. G is observed to decrease at larger I_{beam} values due to a stronger eld effect. The sample shown in (a) exhibited G/G = 63 . Curves obtained before and after I_{ds} V_{ds} sweep measurements under no electron beam exposure are also shown in purple and red, respectively, to demonstrate the absence of device hysteresis. (b) I_{ds} I_{beam} gating curve as a function of V_{ds} for the same device. Transistor on/off ratio, I_{on}/I_{off}, is taken as the ratio of I_{ds} values between the TEM-FET *on* (I_{beam} = 0 nA) and *off* (I_{beam} = 23 nA) *states*, which are indicated in panels (a d). The curve in (b) shows an I_{on}/I_{off} of 2.7. (c) I_{ds} V_{ds} and (d) I_{ds} I_{beam} curves for a different sample showing a higher I_{on}/I_{off} of 56 under a stronger electron beam (70 nA). In (d), the device *off state* is taken as I_{beam} = 70 nA.**

following parameter that reflects the degree of hysteretic behavior:

$$\frac{\Delta G_{hys}}{G}(\%) = \frac{G_{on,prior} - G_{on,after}}{G_{on,prior}}$$

where $G_{on,prior}$ and $G_{on,after}$ correspond to conductances with the electron beam o (I_{beam} = 0 nA) prior to and after electron beam gating (purple and red curves, respectively). As shown in Figure 4a, devices reported until now (Figures 2 and 3) have involved positioning of the electron beam outside of the MoS_2 source drain channel region. The small $\Delta G_{hys}/G$ values (<2) exhibited by these systems are within the detectable noise limit of our measurement system (Supporting Information Figure S6). This indicates that the electron beam gating in these configurations did not a ect the TEM-FET s original conductance once the beam was turned o . In contrast, substantially higher hysteresis is measured when the TEM beam is placed on the channel itself, for example, the device in Figure 4b, which displays $\Delta G_{hys}/G$ = 53 . We attribute this to defect creation by the 200 keV electron beam implemented in this study, which is known to cause the irreversible formation of S vacancies and a degradation in the electronic transport of MoS_2 and WS_2.[19,20,33,34]

In addition to probing electron MoS_2 interactions, we also study the e ect of placing the TEM beam outside of the electron-transparent window (Figure 4d) to highlight the role of suspended SiN_x in producing the gating e ect. As illustrated in Figure 1a, the suspended SiN_x window (orange) containing the source drain channel is encompassed with Si-supported SiN_x (light blue), which acts as a robust device platform (see also Supporting Information Figure S7) and is grounded to the TEM column. Figure 4e,f shows I_{ds} V_{ds} curves when the beam is positioned in these on-window and o -window regions, respectively. Beam placement outside of the window results in no conductance change at all because the underlying Si is relatively conducting and allows charges from electron irradiation to quickly dissipate.[35,36] *In situ* MoS_2 current modulation is therefore possible only when the beam hits the suspended SiN_x window region.

To analyze the e ects of other TEM beam parameters, we probe device conductance while changing diameter d_{beam} of the electron beam to vary the size of the region exposed to electrons (Figure 4g). With the electron beam placed on the SiN_x window at a fixed current (I_{beam} = 23 nA), Figure 4h shows I_{ds} V_{ds} data under tightly focused (green, d_{beam} = 10 nm) and broad beam (gray, d_{beam} = 8.7 m) illumination. A negligible di erence in conductance is observed between the two, suggesting that electronic transport in the TEM-FET is not a ected by the area of interaction between the incident beam and SiN_x window as long as the total beam current is constant. We also note a negligible leakage current (< 500 pA) between the source and drain electrodes through the SiN_x membrane (Figure 4i).

Figure 5 displays *in situ* electronic transport characteristics of a typical TEM-FET device where the electron beam is positioned on the SiN_x window at a distance ~28 m from

https://dx.doi.org/10.1021/acsnano.0c02908
CS Nano 2020 14 7389 7397

the 2D channel (this specific configuration is shown in Figure 1d). Figure 5a contains I_{ds} V_{ds} curves from a MoS_2 channel with I_{beam} from 0 (*i.e.*, electron beam o) to 23 nA. From an initial conductance G = 46 nS at I_{beam} = 0 nA, G drops to 37, 29, 24, and 17 nS for beam currents of 0.5, 3.4, 9.6, and 23 nA, respectively. The maximum conductance drop for this device was $\Delta G/G$ = 63 . Standard error values for G and $\Delta G/G$ that most likely arise from contact resistance in the transport measurement setup or field fluctuations from electromagnetic lenses within the TEM are discussed in Supporting Information Figure S6. The corresponding gating curve showing the dependence of I_{ds} on the electron beam current I_{beam} is given in Figure 5b. Because the current of the electron beam, I_{beam}, controls the current through the MoS_2 device, it can be used as the gating parameter (*i.e.*, x-axis in a conventional I_{ds} V_g transistor gating curve). Therefore, the beam current is here to some extent analogous to the gate voltage applied in a traditional transistor. Here, the transistor is in the "*off state*" when the electron beam current is maximal, I_{beam} = 23 nA, whereas it is in the "*on state*" with its maximum conductance when the beam current is minimal, I_{beam} = 0 nA.

The I_{ds} I_{beam} curves for varying V_{ds} values from 30 to 180 mV show clear transistor characteristics.[37,38] The quality of a FET is conventionally quantified through on/o ratio, I_{on}/I_{off}, which is given by

$$I_{on}/I_{off} = \frac{I_{ds,on}}{I_{ds,off}}$$

where $I_{ds,off(on)}$ is equivalent to I_{ds} when I_{beam} is at maximum (23 nA) and minimum (0 nA) values. The device shown in Figure 5b exhibits an I_{on}/I_{off} of 2.7. Under stronger electron beams, higher levels of gating and drain source current suppression were observed. For example, the TEM-FET displayed in Figure 5c,d under an electron beam current of 70 nA exhibits $\Delta G/G$ = 94 and I_{on}/I_{off} = 56, significantly higher than values obtained under I_{beam} = 23 nA. This suggests that a 3-fold increase of the beam current leads to an increase in I_{on}/I_{off} by about 20 times. Considering that on/o ratios shown in our study are about 5 orders of magnitude below those in conventional MoS_2 FET devices,[38,39] increasing the beam current further is not likely to match the performance of standard back-gated FETs, and at best, a further increase of beam current by few-fold may increase the on/o ratio by a factor of 10 100. It is possible that this gating e ect could be more pronounced by minimizing the contact resistance. Although further studies are needed to elucidate the role of electron voltage and di erent 2D materials, an *in situ* gating platform without the need for extra electrodes or complex geometries presents opportunities for 2D characterization and nanoelectronics.

CONCLUSIONS

In conclusion, we have reported 2D MoS_2-based TEM-FETs that enable concurrent structural characterization with electron microscopy and *in situ* electrical biasing measurements on the same platform. Applying the electron beam to the TEM-FET causes charging of the SiN_x substrate, which leads to a positive surface potential and current suppression in the biased MoS_2 channel. We show that the magnitude of gating is dependent on the electron beam current but largely decoupled from the position and size of the TEM beam. Under SiN_x exposure conditions and electrical gating of the 2D channel, the TEM-FET devices exhibit virtually no device hysteresis, maximum I_{on}/I_{off} values up to 56, and clear transistor-like characteristics. The TEM-FET framework can be easily extended to study the electronic transport properties of nanomaterials together with the atomic resolution structural and analytical capabilities of electron microscopy.

METHODS

MoS_2 Growth. Monolayer MoS_2 was grown using a modified CVD process from a previous work.[40] The 1 (w/w) ammonium heptamolybdate ($(NH_4)_6Mo_7O_{24}$) and sodium cholate ($C_{24}H_{39}NaO_5$) solutions were spin-coated onto 300 nm Si/SiO_2 substrates and loaded into a 1 in. diameter tube furnace with 100 mg of sulfur powder. The furnace was heated to 750 °C for 15 min under a 400 sccm N_2 gas flow and then rapidly cooled to room temperature.

MoS_2 Characterization. PL and Raman measurements were obtained at room temperature in an NTEGRA Spectra system under a 532 nm wavelength (green) excitation and <50 W laser power.[41] An aberration-corrected JEOL 200ARM-CF operating at 200 keV with a high-angle annular dark-field detector was used to acquire STEM images and SAED patterns. STEM images were exposed to an average background subtraction filter to reduce image noise. Additional analysis and detailed defect quantification of pristine MoS_2 material can be found in previous works.[40,42]

Device Fabrication. Sixty micrometer wide electron-transparent windows were first fabricated using conventional photolithography in 100 nm thick LPCVD-deposited low-stress SiN_x sitting on 290 m thick 100⟩ Si substrates (Nova Electronic Materials) with an intrinsic resistivity of 1 10 Ω·cm.[43] The 5/40 nm thick Cr/Au contact pads were then patterned around the windows with physical vapor deposition. CVD-grown monolayer MoS_2 flakes were then transferred to the windows using a KOH-based wet etch procedure and electrically connected to the prepatterned contact pads using electron beam lithography. Al wire bonds then connect these substrates to a custom chip carrier, which is inserted into a 6-lead electrical biasing *in situ* TEM holder (Hummingbird Scientific).[44] Details and images of this workflow can be found in Supporting Information Figure S2.

TEM Experiments. *In situ* measurements were taken with a JEOL F200 operating at 200 keV in HRTEM mode. I_{beam} was varied from 0 to 23 nA by changing the spot size (*i.e.*, strength of CL1) and calibrated using an ammeter connected to the instrument s phosphor screen. A vacuum level of approximately 5 × 10 ^{6} Pa was maintained during experiments. The measurements shown in Figure 5c,d were performed on a JEOL 2010F operating at 200 keV in HRTEM mode with I_{beam} values from 0 to 70 nA.

Transport Measurements. Electronic characterization was performed using two-terminal DC and I_{ds} V_{ds} measurements with a Keithley 2410 SourceMeter. I_{beam}-dependent I_{ds} V_{ds} sweeps were acquired in random order to eliminate sampling bias. Unless otherwise noted, V_{ds} was kept below 200 mV to minimize Joule heating.[17] Measurements were acquired and processed with custom Python and Matlab scripts.

ASSOCIATED CONTENT

Supporting Information

The Supporting Information is available free of charge at https://pubs.acs.org/doi/10.1021/acsnano.0c02908.

Additional details of the TEM-FET fabrication process as well as the full set of data for the location-dependent experiment shown in Figure 3; discussion of electron SiN_x interactions including knock-on collisions (K^+ centers) and radiolysis/thermal excitations; characteristics of electrically isolated MoS_2 flakes, DC measurements of SiN_x membrane charging, and I_{ds} V_{ds} curves/optical images for additional devices; comments on calculated conductance error values (PDF)

https://dx.doi.org/10.1021/acsnano.0c02908
CS Nano 2020 14 7389 7397

AUTHOR INFORMATION

Corresponding Author

Marija rndić *Department of Physics and Astronomy University of Pennsylvania Philadelphia Pennsylvania 19104 United States;* orcid.org/0000 0002 8104 2231; Email: drndic@physics.upenn.edu

Author

Paul Masih as *Department of Physics and Astronomy University of Pennsylvania Philadelphia Pennsylvania 19104 United States;* orcid.org/0000 0003 2644 2280

Complete contact information is available at: https://pubs.acs.org/10.1021/acsnano.0c02908

Notes

The authors declare the following competing financial interest(s): M.D. is consultant and founder of Goeppert (www.gppert.com), that is manufacturing nanotechnology-related products including solid-state and TEM chips, and 2D materials.

ACKNOWLEDGMENTS

Dr. W. Parkin, Dr. J. Rodriguez-Manzo, Dr. A. Balan, and J. P. Thiruraman of the University of Pennsylvania are gratefully acknowledged for their assistance with *in situ* TEM methods and FIB patterning. We also thank Dr. E. Stach and Dr. D. Yates of the University of Pennsylvania for their help with TEM. This work was supported by the National Institutes of Health through Grant No. R21-HG-010536 and by the National Science Foundation through the University of Pennsylvania Materials Research Science and Engineering Center (MRSEC) DMR-1720530, as well as NSF Grant Nos. NSF EFRI 2-DARE 1542707, NSF EAGER 1838456, and NSF DMR 1905045. This work was carried out in part at the Singh Center for Nanotechnology, which is supported by the NSF National Nanotechnology Coordinated Infrastructure Program under Grant No. NNCI-1542153.

REFERENCES

(1) Krivanek, O. L.; Chisholm, M. F.; Nicolosi, V.; Pennycook, T. J.; Corbin, G. J.; Dellby, N.; Murfitt, M. F.; Own, C. S.; Szilagyi, Z. S.; Oxley, M. P.; Pantelides, S. T.; Pennycook, S. J. Atom-By-Atom Structural and Chemical Analysis by Annular Dark-Field Electron Microscopy. *Nature* **2010**, *464*, 571 574.

(2) Susi, T.; Meyer, J. C.; Kotakoski, J. Quantifying Transmission Electron Microscopy Irradiation Effects Using Two-Dimensional Materials. *Nat. Rev. Phys.* **2019**, *1*, 397 405.

(3) Ramachandramoorthy, R.; Bernal, R.; Espinosa, H. D. Pushing the Envelope of *In Situ* Transmission Electron Microscopy. *ACS Nano* **2015**, *9*, 4675 4685.

(4) Hashimoto, A.; Suenaga, K.; Gloter, A.; Urita, K.; Iijima, S. Direct Evidence for Atomic Defects in Graphene Layers. *Nature* **2004**, *430*, 870 873.

(5) Yu, Q.; Jauregui, L. A.; Wu, W.; Colby, R.; Tian, J.; Su, Z.; Cao, H.; Liu, Z.; Pandey, D.; Wei, D.; Chung, T. F.; Peng, P.; Guisinger, N. P.; Stach, E. A.; Bao, J.; Pei, S.-S.; Chen, Y. P. Control and Characterization of Individual Grains and Grain Boundaries in Graphene Grown by Chemical Vapor Deposition. *Nat. Mater.* **2011**, *10*, 443 449.

(6) Masih Das, P.; Danda, G.; Cupo, A.; Parkin, W. M.; Liang, L.; Kharche, N.; Ling, X.; Huang, S.; Dresselhaus, M. S.; Meunier, V.; Drndic, M. Controlled Sculpture of Black Phosphorus Nanoribbons. *ACS Nano* **2016**, *10*, 5687 5695.

(7) Luo, C.; Wang, C.; Wu, X.; Zhang, J.; Chu, J. *In Situ* Transmission Electron Microscopy Characterization and Manipulation of Two-Dimensional Layered Materials beyond Graphene. *Small* **2017**, *13*, 1604259.

(8) Liu, X.; Wood, J. D.; Chen, K. S.; Cho, E.; Hersam, M. C. *In Situ* Thermal Decomposition of Exfoliated Two-Dimensional Black Phosphorus. *J. Phys. Chem. Lett.* **2015**, *6*, 773 778.

(9) Liu, X. H.; Wang, J. W.; Liu, Y.; Zheng, H.; Kushima, A.; Huang, S.; Zhu, T.; Mao, S. X.; Li, J.; Zhang, S.; Lu, W.; Tour, J. M.; Huang, J. Y. *In Situ* Transmission Electron Microscopy of Electrochemical Lithiation, Delithiation and Deformation of Individual Graphene Nanoribbons. *Carbon* **2012**, *50*, 3836 3844.

(10) Sang, X.; Xie, Y.; Yilmaz, D. E.; Lotfi, R.; Alhabeb, M.; Ostadhossein, A.; Anasori, B.; Sun, W.; Li, X.; Xiao, K.; Kent, P. R. C.; van Duin, A. C. T.; Gogotsi, Y.; Unocic, R. R. *In Situ* Atomistic Insight into the Growth Mechanisms of Single Layer 2D Transition Metal Carbides. *Nat. Commun.* **2018**, *9*, 2266.

(11) Zeng, Z.; Zhang, X.; Bustillo, K.; Niu, K.; Gammer, C.; Xu, J.; Zheng, H. *In Situ* Study of Lithiation and Delithiation of MoS_2 Nanosheets Using Electrochemical Liquid Cell Transmission Electron Microscopy. *Nano Lett.* **2015**, *15*, 5214 5220.

(12) Borrnert, F.; Barreiro, A.; Wolf, D.; Katsnelson, M. I.; Buchner, B.; Vandersypen, L. M. K.; Rummeli, M. H. Lattice Expansion in Seamless Bilayer Graphene Constrictions at High Bias. *Nano Lett.* **2012**, *12*, 4455 4459.

(13) Fan, Y.; Robertson, A. W.; Zhou, Y.; Chen, Q.; Zhang, X.; Browning, N. D.; Zheng, H.; Rummeli, M. H.; Warner, J. H. Electrical Breakdown of Suspended Mono- and Few-Layer Tungsten Disulfide *via* Sulfur Depletion Identified by *In Situ* Atomic Imaging. *ACS Nano* **2017**, *11*, 9435 9444.

(14) Kim, T.; Kim, S.; Olson, E.; Zuo, J. *In Situ* Measurements and Transmission Electron Microscopy of Carbon Nanotube Field-Effect Transistors. *Ultramicroscopy* **2008**, *108*, 613 618.

(15) Rodríguez-Manzo, J. A.; Qi, Z. J.; Crook, A.; Ahn, J.-H.; Johnson, A. T. C.; Drndic, M. *In Situ* Transmission Electron Microscopy Modulation of Transport in Graphene Nanoribbons. *ACS Nano* **2016**, *10*, 4004 4010.

(16) Lu, Y.; Merchant, C. A.; Drndic, M.; Johnson, A. T. C. *In Situ* Electronic Characterization of Graphene Nanoconstrictions Fabricated in a Transmission Electron Microscope. *Nano Lett.* **2011**, *11*, 5184 5188.

(17) Qi, Z. J.; Rodríguez-Manzo, J. A.; Botello-Mendez, A. R.; Hong, S. J.; Stach, E. A.; Park, Y. W.; Charlier, J.-C. C.; Drndic, M.; Johnson, A. T. C. Correlating Atomic Structure and Transport in Suspended Graphene Nanoribbons. *Nano Lett.* **2014**, *14*, 4238 4244.

(18) Qi, Z. J.; Daniels, C.; Hong, S. J.; Park, Y. W.; Meunier, V.; Drndic, M.; Johnson, A. T. C. C. Electronic Transport of Recrystallized Freestanding Graphene Nanoribbons. *ACS Nano* **2015**, *9*, 3510 3520.

(19) Parkin, W. M.; Balan, A.; Liang, L.; Das, P. M.; Lamparski, M.; Naylor, C. H.; Rodriguez-Manzo, J. A.; Johnson, A. T. C.; Meunier, V.; Drndic, M. Raman Shifts in Electron-Irradiated Monolayer MoS_2. *ACS Nano* **2016**, *10*, 4134 4142.

(20) Fan, Y.; Robertson, A. W.; Zhang, X.; Tweedie, M.; Zhou, Y.; Rummeli, M. H.; Zheng, H.; Warner, J. H. Negative Electro-Conductance in Suspended 2D WS_2 Nanoscale Devices. *ACS Appl. Mater. Interfaces* **2016**, *8*, 32963 32970.

(21) Mak, K. F.; Lee, C.; Hone, J.; Shan, J.; Heinz, T. F. Atomically Thin MoS_2: A New Direct-Gap Semiconductor. *Phys. Rev. Lett.* **2010**, *105*, 136805.

(22) Li, H.; Zhang, Q.; Yap, C. C. R.; Tay, B. K.; Edwin, T. H. T.; Olivier, A.; Baillargeat, D. From Bulk to Monolayer MoS_2: Evolution of Raman Scattering. *Adv. Funct. Mater.* **2012**, *22*, 1385 1390.

(23) Kappera, R.; Voiry, D.; Yalcin, S. E.; Branch, B.; Gupta, G.; Mohite, A. D.; Chhowalla, M. Phase-Engineered Low-Resistance Contacts for Ultrathin MoS_2 Transistors. *Nat. Mater.* **2014**, *13*, 1128 1134.

(24) Shi, S.; Sun, Z.; Hu, Y. H. Synthesis, Stabilization and Applications of 2-Dimensional 1T Metallic MoS_2. *J. Mater. Chem. A* **2018**, *6*, 23932.

(25) Ahn, J.; Parkin, W. M.; Naylor, C. H.; Johnson, A. T. C.; Drndic, M. Ambient Effects on Electrical Characteristics of CVD-Grown Monolayer MoS_2 Field-Effect Transistors. *Sci. Rep.* **2017**, *7*, 4075.
(26) Pelleg, J. In *Solid Mechanics and Its Applications*; Barber, J., Klarbring, A., Eds.; Springer: New York, 2016; pp 413 444.
(27) Algara-Siller, G.; Kurasch, S.; Sedighi, M.; Lehtinen, O.; Kaiser, U. The Pristine Atomic Structure of MoS_2 Monolayer Protected from Electron Radiation Damage by Graphene. *Appl. Phys. Lett.* **2013**, *103*, 203107.
(28) Egerton, R. F.; Li, P.; Malac, M. Radiation Damage in the TEM and SEM. *Micron* **2004**, *35*, 399 409.
(29) Jiang, N.; Spence, J. C. H. On the Dose-Rate Threshold of Beam Damage in TEM. *Ultramicroscopy* **2012**, *113*, 77 82.
(30) Masih Das, P.; Thiruraman, J. P.; Zhao, M.-Q.; Mandyam, S.; Johnson, A. T. C.; Drndic, M. Atomic-Scale Patterning in Two-Dimensional Van der Waals Superlattices. *Nanotechnology* **2019**, *31*, 105302.
(31) Sharma, V.; Tracy, C.; Schroder, D.; Flores, M.; Dauksher, B.; Bowden, S. Study and Manipulation of Charges Present in Silicon Nitride Films. *IEEE PVSC* **2013**, *39*, 1288 1293.
(32) Chen, K.; Kiriya, D.; Hettick, M.; Tosun, M.; Ha, T.; Madhvapathy, S. R.; Desai, S.; Sachid, A.; Javey, A. Air Stable N-Doping of WSe_2 by Silicon Nitride Thin Films with Tunable Fixed Charge Density. *APL Mater.* **2014**, *2*, 092504.
(33) Komsa, H.; Kurasch, S.; Lehtinen, O.; Kaiser, U.; Krasheninnikov, A. V. From Point to Extended Defects in Two-Dimensional MoS_2: Evolution of Atomic Structure under Electron Irradiation. *Phys. Rev. B: Condens. Matter Mater. Phys.* **2013**, *88*, 035301.
(34) Yoshimura, A.; Lamparski, M.; Kharche, N.; Meunier, V. First-Principles Simulation of Local Response in Transition Metal Dichalcogenides under Electron Irradiation. *Nanoscale* **2018**, *10*, 2388 2397.
(35) Le Gressus, C.; Valin, F.; Gautier, M.; Duraud, J. P.; Cazaux, J.; Okuzumi, H. Charging Phenomena on Insulating Materials: Mechanisms and Applications. *Scanning* **1990**, *12*, 203 210.
(36) Mccartney, M. R. Characterization of Charging in Semiconductor Device Materials by Electron Holography. *J. Electron Microsc.* **2005**, *54*, 239 242.
(37) Chang, H.-Y.; Yang, S.; Lee, J.; Tao, L.; Hwang, W.; Jena, D.; Lu, N.; Akinwande, D. High-Performance, Highly Bendable MoS_2 Transistors with High-K Dielectrics for Flexible Low-Power. *ACS Nano* **2013**, *7*, 5446 5452.
(38) Radisavljevic, B.; Radenovic, A.; Brivio, J.; Giacometti, V.; Kis, A. Single-Layer MoS_2 Transistors. *Nat. Nanotechnol.* **2011**, *6*, 147 150.
(39) Wu, W.; De, D.; Chang, S.-C.; Wang, Y.; Peng, H.; Bao, J.; Pei, S.-S. High Mobility and High On/Off Ratio Field- Effect Transistors Based on Chemical Vapor Deposited Single-Crystal MoS_2 Grains. *Appl. Phys. Lett.* **2013**, *102*, 142106.
(40) Thiruraman, J. P.; Masih Das, P.; Drndic, M. Irradiation of Transition Metal Dichalcogenides Using a Focused Ion Beam: Controlled Single-Atom Defect Creation. *Adv. Funct. Mater.* **2019**, *29*, 1904668.
(41) Danda, G.; Masih Das, P.; Drndic, M. Laser-Induced Fabrication of Nanoporous Monolayer WS_2 Membranes. *2D Mater.* **2018**, *5*, 035011.
(42) Thiruraman, J. P.; Fujisawa, K.; Danda, G.; Das, P. M.; Zhang, T.; Bolotsky, A.; Perea-Lopez, N.; Nicolai, A.; Senet, P.; Terrones, M.; Drndic, M. Angstrom-Size Defect Creation and Ionic Transport through Pores in Single-Layer MoS_2. *Nano Lett.* **2018**, *18*, 1651 1659.
(43) Merchant, C. A.; Healy, K.; Wanunu, M.; Ray, V.; Peterman, N.; Bartel, J.; Fischbein, M. D.; Venta, K.; Luo, Z.; Johnson, A. T. C.; Drndic, M. DNA Translocation through Graphene Nanopores. *Nano Lett.* **2010**, *10*, 2915 2921.
(44) Puster, M.; Rodríguez-Manzo, J. A.; Balan, A.; Drndic, M. Toward Sensitive Graphene Nanoribbon-Nanopore Devices by Preventing Electron Beam-Induced Damage. *ACS Nano* **2013**, *7*, 11283 11289.

https://dx.doi.org/10.1021/acsnano.0c02908
CS Nano 2020 14 7389 7397